Figure 1 Preparation of monolayered MSCs. (a) MSCs 2 d after seeding on a temperature-responsive dish. (b) Cultured MSCs expanded to confluence within the square area of the dish by day 3. (c) The monolayered MSCs detached easily from the culture dish at 20 °C. (d) The completely detached monolayered MSCs were identified as a 12 × 12 mm square sheet. (e–h) Cross-sectional analysis of GFP-expressing monolayered MSCs and DFBs before detachment (e and g, confocal images) and after detachment (f and h, left and center, confocal images; right, Masson trichrome). The thickness of both monolayers was 3.5-fold greater than the thickness before detachment, and constituent cells were compacted. Scale bars in a–c, 100 μm; in d, 5 mm; in e–h, 20 μm.

confirmed that the majority of adherent cells isolated from adipose tissue were MSCs.

Preparation and transplantation of monolayered MSCs

We cultured adipose tissue–derived MSCs (5×10^5 cells) on temperature-responsive dishes for 3 d until confluent. MSCs were attached on the poly-N-isopropylacrylamide (PIPAAm)-grafted area (24 × 24 mm; **Fig. 1a,b**). As the culture temperature was decreased from 37 °C to 20 °C, MSCs detached spontaneously and floated up into the culture medium as a monolayer of MSCs within 40 min (**Fig. 1c,d**). As a control, we prepared dermal fibroblasts (DFBs) by the skin explant technique[27]. DFBs (8×10^5 cells) were cultured on the temperature-responsive dishes, and monolayered DFBs were fabricated as described above. The final cell counts for monolayered MSCs and DFBs before transplantation were $9.4 \pm 0.6 \times 10^5$ and $8.6 \pm 0.6 \times 10^5$ cells, respectively ($n = 6$ each). To identify the thickness of monolayered MSCs, we used green fluorescent protein (GFP)-expressing cell grafts derived from the GFP-transgenic Sprague-Dawley rats. Immediately after detachment, cells became compacted, possibly owing to cytoskeletal tensile reorganization, and the thickness of monolayered MSCs and DFBs was approximately 3.5-fold greater than the thickness before detachment (MSCs, 6.2 ± 0.3 to 21.5 ± 0.8 μm; DFBs, 6.5 ± 0.4 to 22.4 ± 1.1 μm; **Fig. 1e–h**). MSCs on the temperature-responsive dishes were positive for vimentin and slightly positive for collagen type 1, whereas DFBs were positive for both markers (**Fig. 2a**). We transferred detached monolayered MSCs above the myocardial scar (**Fig. 2b**) and then attached them to the surface of the anterior scar (**Fig. 2c**).

Secretion of angiogenic factors from monolayered MSCs

We measured secretion of angiogenic factors from MSCs 24 h after monolayers had formed, equivalent to day 4 after initial cell seeding. The monolayered MSCs secreted significantly larger amounts of angiogenic and antiapoptotic factors such as vascular endothelial growth factor (VEGF) and hepatocyte growth factor (HGF) than did the monolayered DFBs ($P < 0.01$; **Fig. 2d**). The control medium supplemented with 10% fetal calf serum contained less than 5 pg/ml of VEGF or HGF. These results suggest that the paracrine effects of monolayered MSCs on host myocardium are greater than those of monolayered DFBs.

Engraftment and growth of monolayered MSCs

To identify the transplanted cells in myocardial sections, we used GFP-expressing cell grafts derived from the GFP-transgenic Sprague-Dawley rats. We grafted monolayered MSCs or DFBs onto the scar area of the anterior wall (**Fig. 3**). Fluorescence microscopy showed that GFP-expressing monolayered MSCs gradually grew *in situ* and developed into a thick stratum, up to ~600 μm thick over the native tissue at 4 weeks (**Fig. 3a–f**). The engrafted MSC tissue tapered off toward the healthy myocardium (**Fig. 3d,e**), although most of the monolayered MSCs were attached only to the scar area in the anterior wall because of the large infarct. We rarely detected TUNEL-positive MSCs in the sheet (<1%) 48 h after transplantation (**Fig. 3g**), implying that cell viability in the sheet was maintained. In contrast, we frequently detected TUNEL-positive cells (15% ± 2%) in the DFB sheet, which was observed as a thin layer above the scar. Subsequently, the DFB sheet was undetectable 1 week later. Masson trichrome staining showed increased thickness of the anterior wall and attenuation of left ventricle enlargement after transplantation of monolayered MSCs (**Fig. 3h**), although the infarct size did not differ significantly among the untreated, DFB and MSC groups (**Supplementary Table 1** online).

Reconstruction of cardiac mass

After growth *in situ*, GFP-expressing MSC tissue contained a number of mature vascular structures that had positive staining for von Willebrand factor (vWF) and αSMA (**Fig. 4a,b**). A small fraction of the MSC tissue had positive staining for cardiac troponin T and desmin (**Fig. 4c,d**). On the other hand, a large proportion of the MSC tissue was positive for vimentin, a marker for mesenchymal lineage cells (**Fig. 4e**). The percentages of graft-derived cells that expressed endothelial (vWF), smooth muscle (αSMA), cardiac (troponin T) and mesenchymal (vimentin) markers were 12.2% ± 0.6%, 5.0% ± 0.3%, 5.3% ± 0.3% and 57.8% ± 2.2%, respectively. Notably, based on expression of these markers, two-thirds of vascular endothelial cells, four-fifths of smooth muscle cells and one-twentieth of cardiomyocytes within the MSC tissue were GFP⁻ and hence were derived from the host. The MSC tissue stained modestly for collagen type 1 (**Fig. 4f**). Picrosirius red staining showed that collagen deposition was found mainly in the extracellular matrix and the epicardial margin of the MSC tissue (**Fig. 4g**). Excluding staining in blood vessels, the MSC tissue was also negative for αSMA, a marker for myofibroblasts (**Fig. 4b**). This phenotype was consistent with properties of MSCs
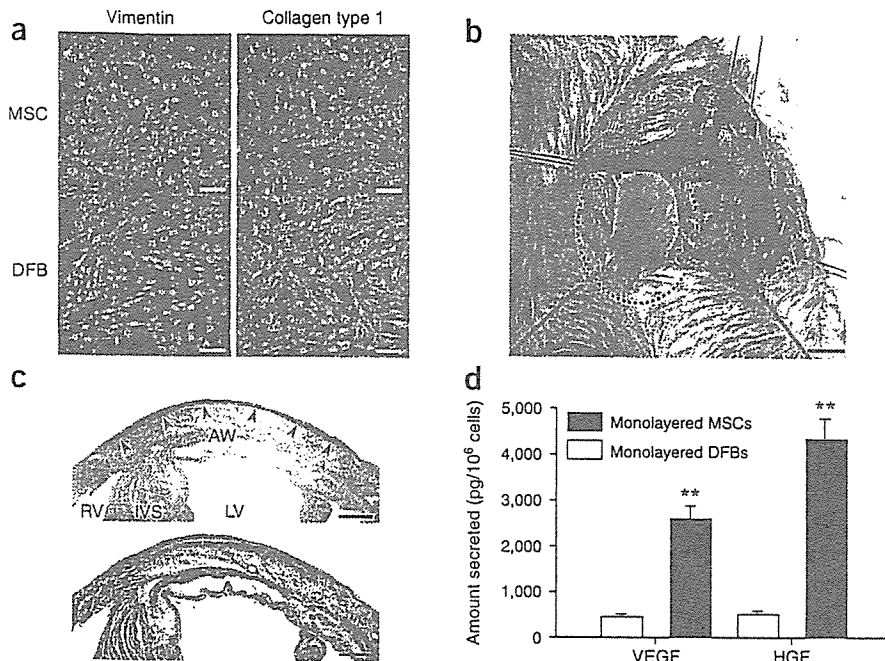
Figure 2 Characteristics of monolayered MSCs. (a) Properties of constituent cells in the monolayered grafts. Compared with DFBs (green), MSCs (green) are positive for vimentin (red) and slightly positive for collagen type 1 (red). (b) Monolayered MSCs (in the dotted circle) transferred to the infarcted heart. (c) Extent of monolayered MSCs 48 h after transplantation (arrows). AW, anterior wall; LV, left ventricle; RV right ventricle; IVS, interventricular septum. (d) Comparison of secretion of growth factors between monolayered MSCs and DFBs. $**P < 0.01$ versus DFBs. Scale bar in a, 20 μm; in b, 5 mm; in c, 100 μm.

before transplantation (**Fig. 2a** and **Supplementary Fig. 1** online), suggesting that the MSC tissue includes a number of undifferentiated MSCs. Taken together, the grown MSC tissue was composed of newly formed blood vessels, undifferentiated MSCs and few cardiomyocytes.

Fluorescence *in situ* hybridization analysis

We performed fluorescence *in situ* hybridization (FISH) to detect X and Y chromosomes after sex-mismatched transplantation of mono-layered MSCs. We transplanted GFP-expressing monolayered MSCs derived from male rats to female Sprague-Dawley rats that had suffered an infarct. Four weeks later, newly formed cardiomyocytes that were positive for GFP had only one set of X and Y chromosomes, whereas we detected two X chromosomes exclusively in GFP⁻ host-derived cells (**Fig. 4h**). We counted the X and Y chromosomes in male and female control rats and in the MSC sheet–transplanted rats (**Supplementary Table 2** online), and we did not detect extra copies of the X or Y chromosome in graft-derived GFP⁺ cardiomyocytes. When we compared the frequencies of the occurrence of zero, one, two and more than two X chromosomes in the GFP⁺ cardiomyocytes with the frequencies in male control cardiomyocytes, the GFP⁺ cardiomyocytes did not show an increased proportion of X chromo-somes ($0.25 > P > 0.10$, χ^2 test).

Effects of monolayered MSCs on cardiac function

Heart failure developed 8 weeks after coronary ligation, as indicated by an increase in left ventricle end-diastolic pressure (LVEDP) and attenuation of maximum and minimum rate of change in left ventricular pressure (dP/dt). Autologous transplantation of mono-layered MSCs, however, resulted in decreased LVEDP (**Fig. 5a**). Left ventricle maximum and minimum dP/dt were significantly improved in the MSC group (**Fig. 5b,c**). We did not observe these hemodynamic improvements in the DFB group. The MSC group also had signifi-cantly lower right ventricular weight and lung weight than the DFB and untreated groups 4 weeks after transplantation (**Supplementary Table 1** online). These results suggest that transplantation of mono-layered MSCs has beneficial hemodynamic effects in rats with chronic heart failure.

Echocardiographic analysis showed that transplantation of monolayered MSCs signi-ficantly increased diastolic thickness of the infarcted anterior wall (**Fig. 5d**). Left ventricle end-diastolic dimension at 8 weeks was sig-nificantly smaller in the MSC group than in the DFB and untreated groups (**Fig. 5e**). Transplantation of the monolayered MSCs significantly increased left ventricle fractional shortening (**Fig. 5f**). Left ventricle wall stress in diastole was markedly lower in the MSC group than in the DFB and untreated groups (**Supplementary Table 3** online). Plasma atrial natriuretic peptide (ANP) in the DFB and untreated groups was markedly elevated 8 weeks after myocardial infarction (**Fig. 5g**). Transplantation of the monolayered MSCs inhibited the increase in plasma ANP.

Survival analysis

The Kaplan-Meier survival curve showed that 4-week survival after coronary ligation did not differ significantly between the untreated and MSC groups before transplantation (**Fig. 5h**). Notably, however, no rats died after transplantation of monolayered MSCs. Therefore, the survival rate after transplantation was markedly higher in the MSC group than in the untreated group (4-week survival after transplanta-tion was 100% for the MSC group versus 71% for the untreated group, log-rank test, $P < 0.05$).

DISCUSSION

There are several advantages to monolayered MSC transplantation. First, the self-propagating property of MSCs *in situ* leads to the formation of a thick stratum on the surface of the scarred myocar-dium. Second, the multipotency of MSCs and their ability to supply angiogenic cytokines allows neovascularization in the MSC tissue. Third, the reconstruction of thick myocardial tissue reduces left ventricle wall stress and results in improvement of cardiac function after myocardial infarction. Finally, a substantial part of the trans-planted tissue is composed of undifferentiated MSCs, and it is tempting to speculate that such cells may act against future progressive left ventricle remodeling.

Cellular cardiomyoplasty using needle injections is emerging as a treatment option for individuals with chronic heart failure, but it may be limited by failure to regenerate cardiac mass. The cell sheet allows for cell-to-cell connections owing to the lack a need for enzymatic digestion[6–10]. Thus, the cell sheet has attracted considerable interest as a tool for tissue engineering[28]. Here, we used adipose tissue–derived MSCs as a cellular source for the cell sheet, which resulted in successful autologous transplantation in heterogenic rats without immunological
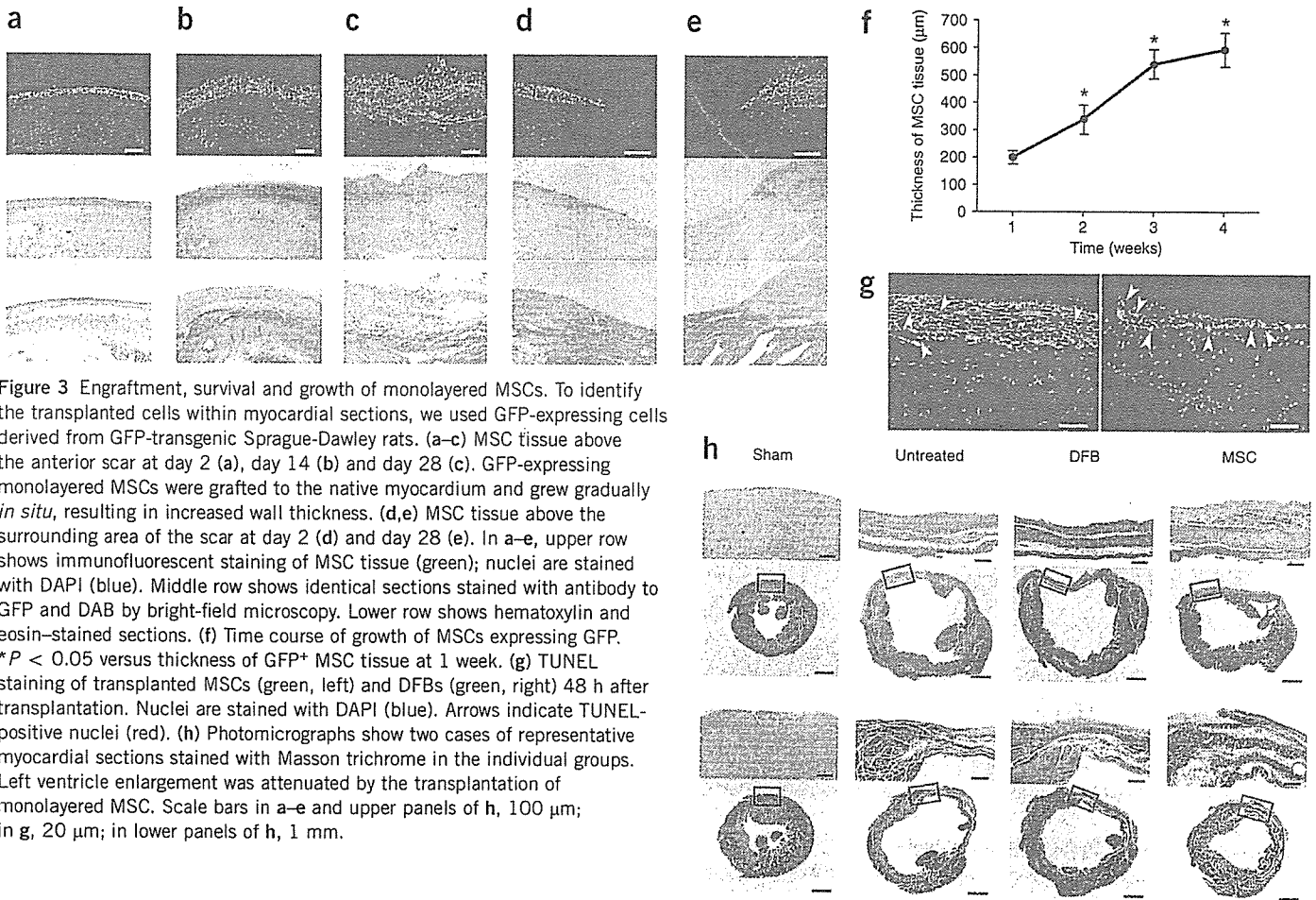
−180−

Figure 3 Engraftment, survival and growth of monolayered MSCs. To identify the transplanted cells within myocardial sections, we used GFP-expressing cells derived from GFP-transgenic Sprague-Dawley rats. (a–c) MSC tissue above the anterior scar at day 2 (a), day 14 (b) and day 28 (c). GFP-expressing monolayered MSCs were grafted to the native myocardium and grew gradually *in situ*, resulting in increased wall thickness. (d,e) MSC tissue above the surrounding area of the scar at day 2 (d) and day 28 (e). In a–e, upper row shows immunofluorescent staining of MSC tissue (green); nuclei are stained with DAPI (blue). Middle row shows identical sections stained with antibody to GFP and DAB by bright-field microscopy. Lower row shows hematoxylin and eosin–stained sections. (f) Time course of growth of MSCs expressing GFP. *P < 0.05 versus thickness of GFP+ MSC tissue at 1 week. (g) TUNEL staining of transplanted MSCs (green, left) and DFBs (green, right) 48 h after transplantation. Nuclei are stained with DAPI (blue). Arrows indicate TUNEL-positive nuclei (red). (h) Photomicrographs show two cases of representative myocardial sections stained with Masson trichrome in the individual groups. Left ventricle enlargement was attenuated by the transplantation of monolayered MSC. Scale bars in a–e and upper panels of h, 100 μm; in g, 20 μm; in lower panels of h, 1 mm.

rejection. Using flow cytometry, we did not find any substantial differences between adipose tissue–derived MSCs and bone marrow–derived MSCs, consistent with results from previous studies[22,25]. Adipose-derived MSCs readily attached to and propagated on the temperature-responsive dish. Abdominal subcutaneous adipose tissue is clinically redundant and easily accessible by rapid and minimally invasive surgery such as liposuction. Thus, adipose tissue may serve as a source of stem cells for therapeutic cell sheets.

Here, monolayered MSCs could readily be transferred and grafted to the scarred myocardium without additives or suturing. This may be attributable to cell-to-cell connections as well as extracellular matrix deposits on the basal surface of the monolayered MSCs. Regeneration of myocardial mass is thought to require multilayered constructs of the cell sheet. Unfortunately, however, the lack of a vascular network has limited the formation of a thick construct[10,29]. The transplanted monolayered MSCs thickened gradually, developing into a stratum of up to 600 μm in thickness over the native tissue 4 weeks after transplantation, suggesting that monolayered MSCs have an ability to grow *in situ*. As a result, the transplanted MSC tissue reversed wall thinning of the infarcted myocardium. On the other hand, the fibroblast sheet did not grow *in situ*. It should be noted that the MSC tissue included a large number of newly formed blood vessels. These vessels were composed of graft-derived cells, host-derived cells or both. The MSC sheet secreted a large amount of angiogenic and antiapoptotic cytokines, including VEGF and HGF, as compared with the fibroblast sheet. These results suggest that MSCs induce neovascularization within the sheet not only through their ability to differentiate into vascular cells but also through growth factor–mediated paracrine

regulation. Thus, we believe that the angiogenic action of MSCs is important for reconstruction of cardiac mass by the MSC tissue.

Four weeks after transplantation, a small fraction of the engrafted MSCs were positive for cardiac proteins such as cardiac troponin T and desmin, suggesting the presence of cardiomyocytes within the MSC tissue. FISH analysis suggested that the most cardiomyocytes within the MSC tissue were not derived from cell fusion, but we are unable to exclude the possibility that some were. Further studies are necessary to investigate the mechanisms by which MSCs within the MSC tissue regenerate cardiomyocytes. The majority of the MSC tissue was positive for vimentin, a marker for undifferentiated MSCs and fibroblasts. In addition, the majority of MSCs within the graft were negative for collagen type 1 and αSMA, a marker for myofibroblasts. These results suggest that the grown-up MSC tissue is composed of newly formed blood vessels, undifferentiated MSCs and few cardiomyocytes.

We have also shown that transplantation of the monolayered MSCs significantly increased left ventricle maximum dP/dt, decreased LVEDP and inhibited the development of left ventricle enlargement in rats with chronic heart failure secondary to myocardial infarction. These results suggest that transplantation of monolayered MSCs improves cardiac function. But the presence of cardiomyocytes within the MSC tissue seemed to be rare. Thus, this improvement may be explained mainly by growth factor–mediated paracrine effects of the MSC sheet and a decrease in left ventricle wall stress resulting from the thick MSC tissue. Furthermore, no rats treated with the monolayered MSCs died during the study period, although untreated rats died frequently. These results indicate that fatal arrythmogenic problems were not caused by integration of the MSC tissue.
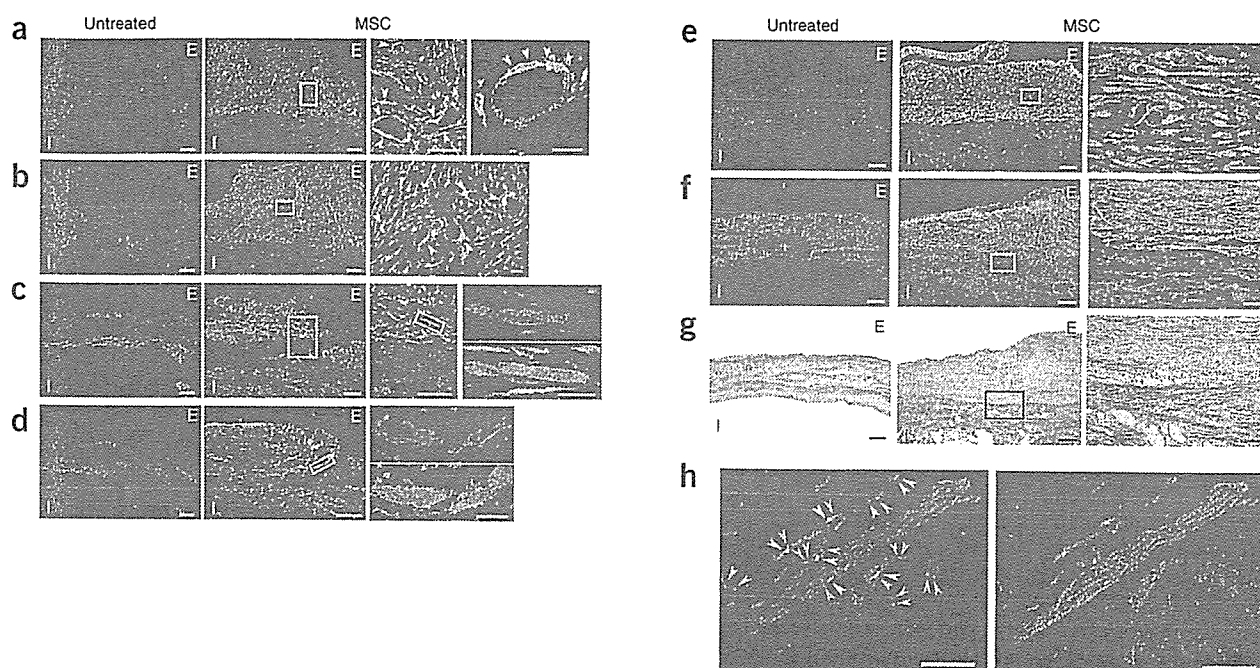
Figure 4 Differentiation of MSCs within the MSC tissue after growth *in situ*. (a,b) GFP-expressing MSCs (green) were identified as a thick stratum at the epicardial side of the myocardium. The MSC tissue contained a number of vascular structures positive for vWF (red, a) and αSMA (red, b). MSCs that did not participate in blood vessel formation were only rarely positive for αSMA, a marker for myofibroblasts. Arrows indicate transplanted MSCs positive for vWF or αSMA. (c,d) Some MSCs within the MSC tissue were positive for cardiac markers cardiac troponin T (red, c) and desmin (red, d). (e) Most of the MSC tissue was positive for vimentin (red). (f) The MSC tissue modestly stained for collagen type 1 (red). (g) Collagen deposition was also detected by picrosirius red staining. (h) FISH analysis. Newly formed cardiomyocytes (desmin, red) that were positive for GFP (green) had only one set of X (purple) and Y chromosomes (white), whereas two X chromosomes were detected exclusively in GFP⁻ host-derived cells. Nuclei are stained with DAPI (blue, a–f and h). Scale bars in left three panels of a and c and in two left panels of b and d–g, 100 μm; in h and far right panels of a–g, 20 μm. E, epicardial side; I, intimal side.

In summary, adipose tissue–derived monolayered MSCs can be readily engrafted to the scarred myocardium, grow gradually *in situ* and become a thick stratum that includes newly formed vessels, cardiomyocytes and undifferentiated MSCs. The engrafted MSCs reversed wall thinning in the scar area and improved cardiac function and survival in rats with myocardial infarction. Thus, transplantation of monolayered MSCs may be a new therapeutic strategy for cardiac tissue regeneration.

METHODS

Model of heart failure. All protocols were performed in accordance with the guidelines of the Animal Care Ethics Committee of the Japanese National Cardiovascular Center Research Institute. We used male Sprague-Dawley rats (Japan SLC) weighing 187–215 g. A myocardial infarction model was produced by ligation of the left coronary artery, as described previously[30]. Briefly, we anesthetized rats with sodium pentobarbital (30 mg/kg) and ventilated them with a volume-regulated respirator. We exposed hearts by left thoracotomy, and ligated the left coronary artery 2–3 mm from its origin between the pulmonary artery conus and the left atrium with a 6-0 Prolene suture. The sham group underwent thoracotomy and cardiac exposure without coronary ligation. The surviving rats were maintained on standard rat chow.

Study protocol. We randomly placed rats into four groups: rats with chronic heart failure that underwent transplantation of monolayered MSCs (MSC group; n = 12), rats with chronic heart failure given monolayered DFBs (DFB group; n = 12), rats with chronic heart failure without transplantation (untreated group; n = 12) and sham-operated rats without transplantation (sham group; n = 10). Four weeks after coronary ligation, the MSC and DFB groups underwent autologous transplantation of each monolayered cell graft onto the anterior wall, including the scar area (Supplementary Methods online). The other two groups underwent the same operative procedures

without transplantation. We performed hemodynamic studies, echocardiography and histological assessments 4 and 8 weeks after coronary ligation (Supplementary Methods). Upon killing at 8 weeks after coronary ligation, only those rats with infarct size > 25% of the left ventricle area were included in this study. Therefore, the variation in infarct size between the experimental rats was relatively low (28–41%, average 33.9% ± 1.9%).

Isolation and culture of MSCs from adipose tissue. Immediately after coronary ligation, we acquired subcutaneous adipose tissue (1.1 ± 0.1 g) from the right inguinal region of each rat. We minced adipose tissue with scissors and digested it with 10 ml of type 1 collagenase solution (0.1 mg/ml, Worthington Biochemical) for 1 h in a 37 °C water bath shaker. After filtration with mesh filter (Costar 3480, Corning) and centrifugation at 780g for 8 min, we suspended isolated cells in α-MEM supplemented with 10% FCS and antibiotics, plated them onto a 100-mm dish and incubated them at 37 °C with 5% CO_2. A small number of spindle-shaped cells were apparent in visible symmetric colonies by days 5–7.

Preparation of temperature-responsive dishes. Specific procedures for preparation of square-designed PIPAAm-grafted dishes have been previously described[9]. Briefly, we spread IPAAm monomer (Kohjin) in 2-propanol solution onto 60-mm polystyrene culture dishes (Corning). We then subjected the dishes to irradiation (0.25-MGy electron beam dose) using an Area Beam Electron Processing system (Nisshin High-Voltage) to immobilize IPAAm on the dish surface; we then rinsed dishes with cold distilled water and dried them in nitrogen gas. In the second step, we masked the PIPAAm-grafted surface with a square glass coverslip (24 × 24 mm, Matsunami Glass). We spread acrylamide (AAm) monomer solution in 2-propanol onto the masked dish surface. We then irradiated the dish surface with an electron beam and washed it. As a result, the central square area of each dish was PIPAAm grafted (temperature responsive), and the surrounding border was poly-AAm grafted (non–cell adhesive). This PIPAAm-grafted surface is hydrophobic under culture
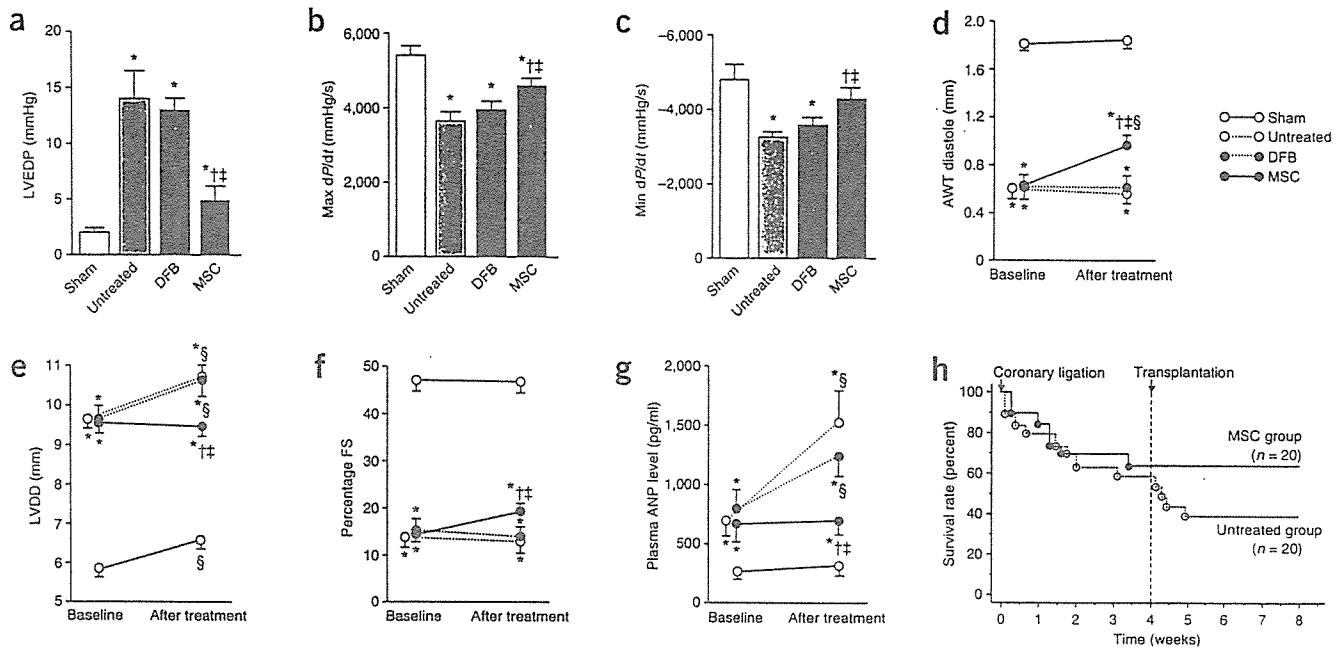
–182–

Figure 5 Cardiac structure and function after transplantation of monolayered MSCs. (a–c) Hemodynamic parameters obtained by catheterization. LVEDP, left ventricle end-diastolic pressure. (d–f) Echocardiographic findings. AWT, anterior wall thickness; LVDD, left ventricle end-diastolic dimension; FS, fractional shortening. (g) Plasma atrial natriuretic peptide (ANP) level. Baseline represents measurements 4 weeks after coronary ligation; 'after treatment' represents measurements taken 4 weeks after transplantation (8 weeks after coronary ligation). Data are mean ± s.e.m. *$P < 0.05$ versus sham group; †$P < 0.05$ versus untreated group; ‡$P < 0.05$ versus DFB group; §$P < 0.05$ versus baseline. (h) Survival of rats with chronic heart failure with or without monolayered MSC transplantation. The Kaplan-Meier survival curve demonstrates an 8-week survival rate of 65% for the MSC group versus 45% for the untreated group. Survival rate after transplantation was significantly higher in the MSC group than in the untreated group (100% versus 71% 4-week survival rate after transplantation, log-rank test, $P < 0.05$).

conditions at 37 °C and becomes reversibly hydrophilic below 32 °C. Therefore, cultured cells that adhere to the dish surface spontaneously detach from the grafted surface without enzymatic digestion.

Preparation of monolayered cell grafts. We suspended MSCs at the third or fourth passage from adipose tissue or DFBs at the second passage by trypsinization, and plated the cell suspension containing 3 ml of complete medium onto a 60-mm temperature-responsive dish at 5×10^5 cells per dish (MSCs) or 8×10^5 cells per dish (DFBs) and cultured cells at 37 °C. After 3 d of culture, confluently cultured MSCs or DFBs on the temperature-responsive dishes were incubated at 20 °C. By 40 min, both MSCs and DFBs detached spontaneously and floated up into the medium as monolayered cell grafts. Immediately after detachment, we gently aspirated the monolayered cell grafts using a 1,000 µl pipette tip and transferred them onto an elastic plastic sheet.

Statistical analysis. Numerical values are expressed as mean ± s.e.m. There are four groups of continuous variables in this study. Therefore, for multiple comparisons of more than two groups, we performed one-way analysis of variance (ANOVA). If the ANOVA was significant, we used the Newman-Keul procedure as a *post hoc* test. For repeated measurement such as echocardiographic parameters, we performed two-way repeated ANOVA with the Newman-Keul test. Comparisons of parameters between two groups were made by unpaired Student *t*-test. A value of $P < 0.05$ was considered significant.

Note: Supplementary information is available on the Nature Medicine website.

COMPETING INTERESTS STATEMENT
The authors declare competing financial interests (see the *Nature Medicine* website for details).

Published online at http://www.nature.com/naturemedicine/
Reprints and permissions information is available online at http://npg.nature.com/reprintsandpermissions/

1. Liu, J. *et al.* Autologous stem cell transplantation for myocardial repair. *Am. J. Physiol. Heart Circ. Physiol.* **287**, H501–H511 (2004).
2. Reinlib, L. & Field, L. Cell transplantation as future therapy for cardiovascular disease?: A workshop of the National Heart, Lung, and Blood Institute. *Circulation* **101**, E182–E187 (2000).
3. Schuster, M.D. *et al.* Myocardial neovascularization by bone marrow angioblasts results in cardiomyocyte regeneration. *Am. J. Physiol. Heart Circ. Physiol.* **287**, H525–H532 (2004).
4. Kocher, A.A. *et al.* Neovascularization of ischemic myocardium by human bone-marrow-derived angioblasts prevents cardiomyocyte apoptosis, reduces remodeling and improves cardiac function. *Nat. Med.* **7**, 430–436 (2001).
5. Bel, A. *et al.* Transplantation of autologous fresh bone marrow into infarcted myocardium: a word of caution. *Circulation* **108**, II247–II252 (2003).
6. Yamada, N. *et al.* Thermo-responsive polymeric surface: control of attachment and detachment of cultured cells. *Makromol. Chem. Rapid Commun.* **11**, 571–576 (1990).
7. Okano, T., Yamada, H., Sakai, H. & Sakurai, Y. A novel recovery system for cultured cells using plasma-treated polystyrene dishes grafted with poly (N-isopropylacrylamide). *J. Biomed. Mater. Res.* **27**, 1243–1251 (1993).
8. Shimizu, T. *et al.* Fabrication of pulsatile cardiac tissue grafts using a novel 3-dimensional cell sheet manipulation technique and temperature-responsive cell culture surfaces. *Circ. Res.* **90**, e40–e48 (2002).
9. Hirose, M., Kwon, O.H., Yamato, M., Kikuchi, A. & Okano, T. Creation of designed shape cell sheets that are noninvasively harvested and moved onto another surface. *Biomacromolecules* **1**, 377–381 (2000).
10. Kushida, A. *et al.* Decrease in culture temperature releases monolayer endothelial cell sheets together with deposited fibronectin matrix from temperature-responsive culture surfaces. *J. Biomed. Mater. Res.* **45**, 355–362 (1999).
11. Herreros, J. *et al.* Autologous intramyocardial injection of cultured skeletal muscle-derived stem cells in patients with non-acute myocardial infarction. *Eur. Heart J.* **24**, 2012–2020 (2003).

12. Skobel, E. *et al.* Transplantation of fetal cardiomyocytes into infarcted rat hearts results in long-term functional improvement. *Tissue Eng.* 10, 849–864 (2004).

13. Hodgson, D.M. *et al.* Stable benefit of embryonic stem cell therapy in myocardial infarction. *Am. J. Physiol. Heart Circ. Physiol.* 287, H471–H479 (2004).

14. Makino, S. *et al.* Cardiomyocytes can be generated from marrow stromal cells in vitro. *J. Clin. Invest.* 103, 697–705 (1999).

15. Pittenger, M.F. *et al.* Multilineage potential of adult human mesenchymal stem cells. *Science* 284, 143–147 (1999).

16. Reyes, M. *et al.* Origin of endothelial progenitors in human postnatal bone marrow. *J. Clin. Invest.* 109, 337–346 (2002).

17. Toma, C., Pittenger, M.F., Cahill, K.S., Byrne, B.J. & Kessler, P.D. Human mesenchymal stem cells differentiate to a cardiomyocyte phenotype in the adult murine heart. *Circulation* 105, 93–98 (2002).

18. Wang, J.S. *et al.* Marrow stromal cells for cellular cardiomyoplasty: feasibility and potential clinical advantages. *J. Thorac. Cardiovasc. Surg.* 120, 999–1005 (2000).

19. Jiang, Y. *et al.* Pluripotency of mesenchymal stem cells derived from adult marrow. *Nature* 418, 41–49 (2002).

20. Nagaya, N. *et al.* Transplantation of mesenchymal stem cells improves cardiac function in a rat model of dilated cardiomyopathy. *Circulation* 112, 1128–1135 (2005).

21. Rangappa, S., Fen, C., Lee, E.H., Bongso, A. & Wei, E.S. Transformation of adult mesenchymal stem cells isolated from the fatty tissue into cardiomyocytes. *Ann. Thorac. Surg.* 75, 775–779 (2003).

22. Zuk, P.A. *et al.* Human adipose tissue is a source of multipotent stem cells. *Mol. Biol. Cell* 13, 4279–4295 (2002).

23. Gaustad, K.G., Boquest, A.C., Anderson, B.E., Gerdes, A.M. & Collas, P. Differentiation of human adipose tissue stem cells using extracts of rat cardiomyocytes. *Biochem. Biophys. Res. Commun.* 314, 420–427 (2004).

24. Planat-Benard, V. *et al.* Plasticity of human adipose lineage cells toward endothelial cells: physiological and therapeutic perspectives. *Circulation* 109, 656–663 (2004).

25. Lee, R.H. *et al.* Characterization and expression analysis of mesenchymal stem cells from human bone marrow and adipose tissue. *Cell. Physiol. Biochem.* 14, 311–324 (2004).

26. Li, J., Takaishi, K., Cook, W., McCorkle, S.K. & Unger, R.H. Insig-1 "brakes" lipogenesis in adipocytes and inhibits differentiation of preadipocytes. *Proc. Natl. Acad. Sci. USA* 100, 9476–9481 (2003).

27. Vande Berg, J.S., Rudolph, R. & Woodward, M. Comparative growth dynamics and morphology between cultured myofibroblasts from granulating wounds and dermal fibroblasts. *Am. J. Pathol.* 114, 187–200 (1984).

28. Nishida, K. *et al.* Corneal reconstruction with tissue-engineered cell sheets composed of autologous oral mucosal epithelium. *N. Engl. J. Med.* 351, 1187–1196 (2004).

29. Shimizu, T., Yamato, M., Kikuchi, A. & Okano, T. Cell sheet engineering for myocardial tissue reconstruction. *Biomaterials* 24, 2309–2316 (2003).

30. Nishikimi, T., Uchino, K. & Frohlich, E.D. Effects of $\alpha 1$-adrenergic blockade on intrarenal hemodynamics in heart failure rats. *Am. J. Physiol. Regul. Integr. Comp. Physiol.* 262, R198–R203 (1998).

K-edge angiography utilizing a tungsten plasma X-ray generator in conjunction with gadolinium-based contrast media

Eiichi Sato[a,*], Yasuomi Hayasi[a], Etsuro Tanaka[b], Hidezo Mori[c], Toshiaki Kawai[d], Takashi Inoue[e], Akira Ogawa[e], Shigehiro Sato[f], Kazuyoshi Takayama[g], Jun Onagawa[h], Hideaki Ido[h]

[a]Department of Physics, Iwate Medical University, 3-16-1 Honchodori, Morioka 020-0015, Japan
[b]Department of Nutritional Science, Faculty of Applied Bio-science, Tokyo University of Agriculture, 1-1-1 Sakuragaoka, Setagaya-ku 156-8502, Japan
[c]Department of Cardiac Physiology, National Cardiovascular Center Research Institute, 5-7-1 Fujishirodai, Suita, Osaka 565-8565, Japan
[d]Electron Tube Division #2, Hamamatsu Photonics K. K., 314-5 Shimokanzo, Iwata 438-0193, Japan
[e]Department of Neurosurgery, School of Medicine, Iwate Medical Universichimaru, Morioka 020-8505, Japan
[f]Department of Microbiology, School of Medicine, Iwate Medical University, 19-1 Uchimaru, Morioka 020-8505, Japan
[g]Shock Wave Research Center, Institute of Fluid Science, Tohoku University, 2-1-1 Katahira, Sendai 980-8577, Japan
[h]Department of Applied Physics and Informatics, Faculty of Engineering, Tohoku Gakuin University, 1-13-1 Chuo, Tagajo 985-8537, Japan

Abstract

The tungsten plasma flash X-ray generator is useful in order to perform high-speed enhanced K-edge angiography using cone beams because K-series characteristic X-rays from the tungsten target are absorbed effectively by gadolinium-based contrast media. In the flash X-ray generator, a 150 nF condenser is charged up to 80 kV by a power supply, and flash X-rays are produced by the discharging. The X-ray tube is a demountable diode, and the turbomolecular pump evacuates air from the tube with a pressure of approximately 1 mPa. Since the electric circuit of the high-voltage pulse generator employs a cable transmission line, the high-voltage pulse generator produces twice the potential of the condenser charging voltage. At a charging voltage of 80 kV, the estimated maximum tube voltage and current were approximately 160 kV and 40 kA, respectively. When the charging voltage was increased, the characteristic X-ray intensities of tungsten K_α lines increased. The K_α lines were clean, and hardly any bremsstrahlung rays were detected. The X-ray pulse widths were approximately 110 ns, and the time-integrated X-ray intensity had a value of approximately 0.35 mGy at 1.0 m from the X-ray source with a charging voltage of 80 kV. Angiography was performed

*Corresponding author.
E-mail address: dresato@iwate-med.ac.jp (E. Sato).

using a film-less computed radiography (CR) system and gadolinium-based contrast media. In angiography of non-living animals, we observed fine blood vessels of approximately 100 μm with high contrasts.

1. Introduction

The successful uses of monochromatic parallel beams from synchrotron orbital radiation in recent years have greatly increased the demand for phase-contrast radiography (Davis et al., 1995; Momose et al., 1996; Ando et al., 2002) and enhanced K-edge angiography (Thompson et al., 1992; Mori et al., 1996; Hyodo et al., 1998). In particular, the parallel beams with photon energies of approximately 35 keV have been employed to perform angiography, because the beams are absorbed effectively by iodine-based contrast media with a K-absorption edge of 33.2 keV. Without using a synchrotron, we have developed an X-ray generator utilizing a cerium-target tube, and have performed cone-beam K-edge angiography achieved with cerium K_α rays of 34.6 keV (Sato et al., 2004a, b, c).

Gadolinium-based contrast media with a K-edge of 50.2 keV have been employed to perform magnetic resonance angiography (MRA), and the gadolinium density has been increasing. In view of this situation, ytterbium K_α rays (52.0 keV) are useful for enhanced K-edge angiography, because the K_α rays are absorbed effectively by gadolinium media. As compared with angiography using iodine media, the absorbed dose can be decreased considerably utilizing angiography achieved with gadolinium media. However, because ytterbium is a lanthanide series element and tends to oxidize in the atmosphere, K_α rays of tantalum (57.1 keV) and tungsten (58.9 keV) are also useful to perform angiography.

To produce high-dose-rate X-rays, several different flash X-ray generators have been developed (Sato et al., 1990, 1994a, b; Shikoda et al., 1994; Takahashi et al., 1994), and plasma flash X-ray generators (Sato et al., 2003a, b, 2004a, b, c, 2005a, b, c) have been developed to perform a preliminary experiment for producing hard X-ray lasers. In the plasma, the bremsstrahlung X-rays are absorbed effectively and are converted into fluorescent rays, and intense and clean K-series characteristic X-rays of nickel and copper have been produced from the axial direction of weakly ionized linear plasma. However, it is difficult to increase the photon energies of characteristic X-rays because the plasma transmits high-photon-energy bremsstrahlung X-rays. In view of this situation, we have developed a compact flash X-ray generator (Sato et al., 2004a, b, c, 2005a, b, c) and have succeeded in producing clean high-photon-energy characteristic X-rays utilizing the angle dependence of bremsstrahlung X-rays, because bremsstrahlung rays are not emitted in the opposite direction to that of electron trajectory in Sommerfeld's theory.

In this article, we describe an intense quasi-monochromatic plasma flash X-ray generator with a tungsten target tube, and used it to perform a preliminary study on angiography achieved with tungsten K_α rays.

2. Principle of K-edge angiography

Fig. 1 shows the mass attenuation coefficients of gadolinium at the selected energies; the coefficient curve is discontinuous at the gadolinium K-edge. The average photon energy of the tungsten K_α lines is shown above the gadolinium K-edge. The average photon energy is 58.9 keV, and gadolinium contrast media with a K-absorption edge of 50.2 keV absorb the lines easily. Therefore, blood vessels were observed with high contrasts.
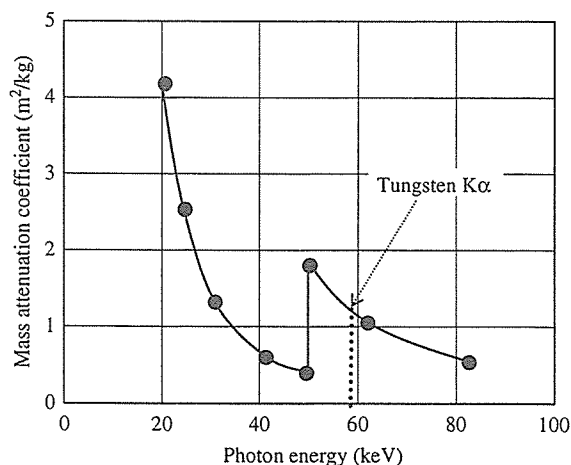

Fig. 1. Mass attenuation coefficients of gadolinium. The average photon energy of tungsten K_α lines is shown above gadolinium K edge.
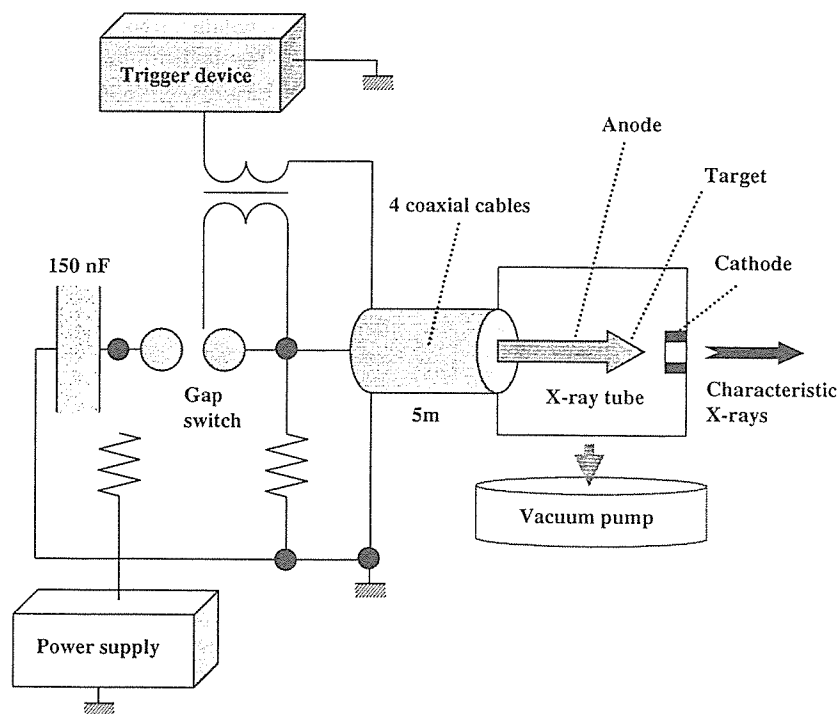
Fig. 2. Block diagram including the high-voltage circuit of the intense quasi-monochromatic plasma flash X-ray generator with a tungsten-target tube.
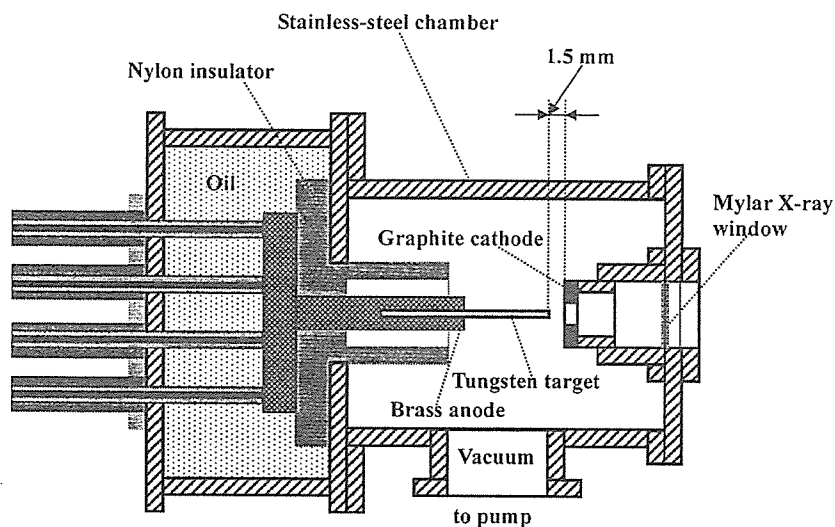

Fig. 3. Schematic drawing of a flash X-ray tube with a rod-shaped tungsten target.

3. Generator

3.1. High-voltage circuit

Fig. 2 shows a block diagram of a high-intensity plasma flash X-ray generator. The generator consists of the following essential components: a high-voltage power supply, a high-voltage condenser with a capacity of approximately 150 nF, an air gap switch, a turbomolecular pump, a thyratron pulse generator as a trigger device and a flash X-ray tube. In this generator, a coaxial cable transmission line is employed in order to
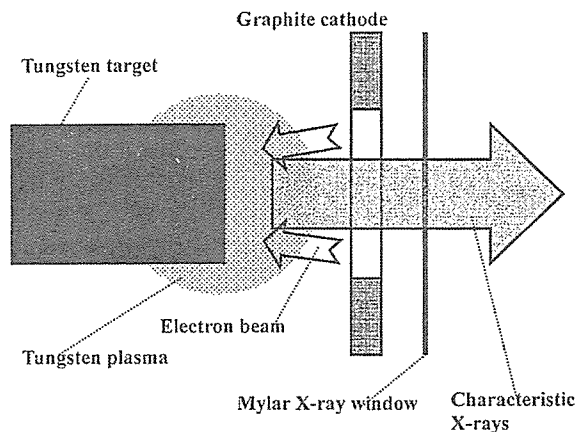
Fig. 4. Irradiation of K-series characteristic X-rays of tungsten.

increase maximum tube voltage using high-voltage reflection. The high-voltage main condenser is charged up to 80 kV by the power supply, and electric charges in the condenser are discharged to the tube through the four cables after closing the gap switch with the trigger device.

3.2. X-ray tube

The X-ray tube is a demountable cold-cathode diode that is connected to the turbomolecular pump with a pressure of approximately 1 mPa (Fig. 3). This tube consists of the following major parts: a ring-shaped graphite cathode with an inside diameter of 4.5 mm, a stainless-steel vacuum chamber, a nylon insulator, a polyethylene terephthalate (Mylar) X-ray window 0.25 mm in thickness and a rod-shaped tungsten target 3.0 mm in diameter. The distance between the target and cathode electrodes can be regulated from the outside of the tube, and is set to 1.5 mm. As electron beams from the cathode electrode are roughly converged to the target by the electric field in the tube, evaporation leads to the formation of weakly ionized plasma, consisting of tungsten ions and electrons, around the target. Because bremsstrahlung rays are not emitted in the opposite direction to that of electron trajectory (Fig. 4), tungsten K-series characteristic X-rays can be produced without using a filter.

4. Characteristics

4.1. Tube voltage and current

In this generator, it was difficult to measure the tube voltage and current since the tube voltages were high, and there was no space to set a current transformer for measuring the tube current. Currently, the voltage and

Fig. 5. X-ray outputs detected using a combination of a plastic scintillator and a photomultiplier.
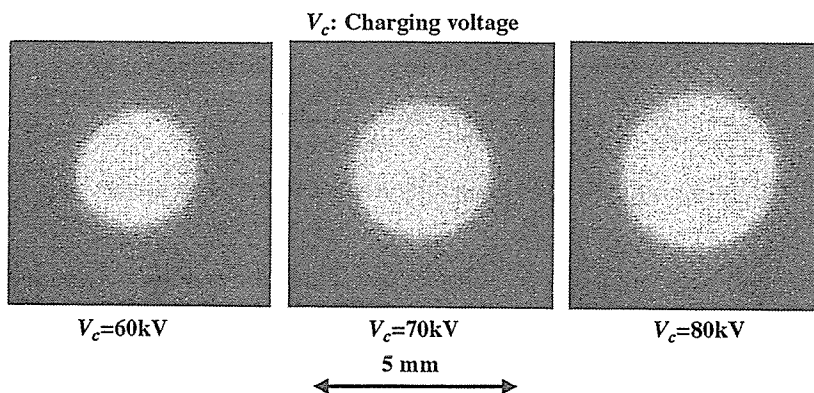

Fig. 6. Images of characteristic X-ray source obtained using a pinhole camera with changes in the charging voltage.
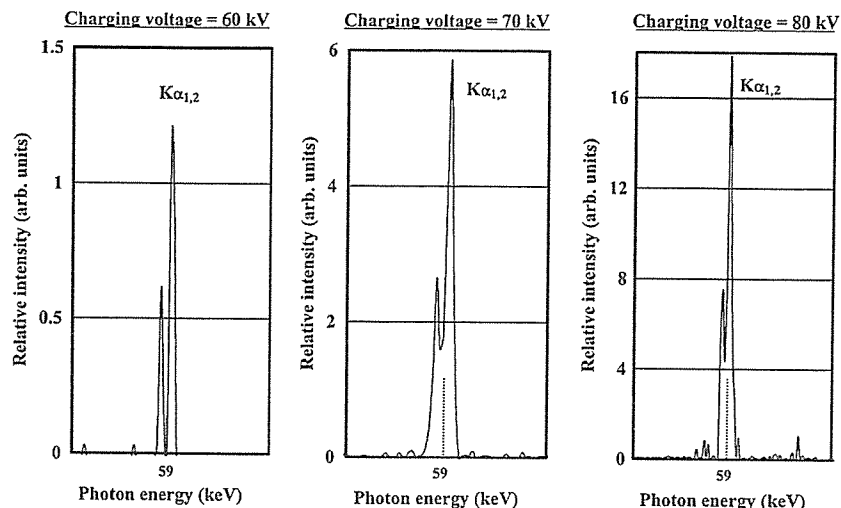
Fig. 7. X-ray spectra from a tungsten target. The spectra were measured using a transmission type spectrometer with a lithium fluoride curved crystal.
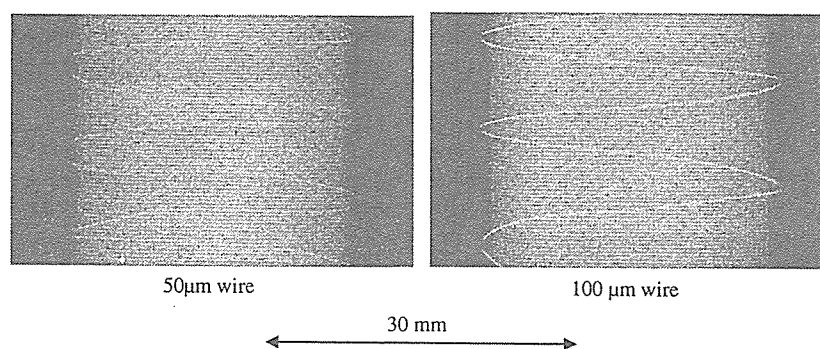

Fig. 8. Radiograms of tungsten wires coiled around rods made of polymethyl methacrylate.

current roughly display damped oscillations. When the charging voltage was increased, both the maximum tube voltage and current increased. At a charging voltage of 80 kV, the estimated maximum values of the tube voltage and current were approximately 160 kV (two times the charging voltage) and 40 kA, respectively.

4.2. X-ray output

X-ray output pulse was detected using a combination of a plastic scintillator and a photomultiplier (Fig. 5). The X-ray pulse height substantially increased with corresponding increases in the charging voltage. The X-ray pulse widths were approximately 110 ns, and the time-integrated X-ray intensity measured by a thermoluminescence dosimeter (Kyokko TLD Reader 1500 having MSO-S elements without energy compensation) had a value of approximately 0.35 mGy at 1.0 m from the X-ray source with a charging voltage of 80 kV.

4.3. X-ray source

In order to observe the plasma X-ray source, we employed a 100-μm-diameter pinhole camera and an X-ray film (Polaroid XR-7) (Fig. 6). When the charging voltage was increased, the plasma X-ray source grew, and both spot dimension and intensity increased. Because the X-ray intensity is the highest at the center of the spot, both the dimension and intensity decreased according to both increases in the thickness of a filter for absorbing X-rays and decreases in the pinhole diameter.

4.4. X-ray spectra

X-ray spectra were measured using a transmission-type spectrometer with a lithium fluoride curved crystal 0.5 mm in thickness. The X-ray intensities of the spectra were detected by an imaging plate of a computed radiography (CR) system (Sato et al., 2000) (Konica Minolta Regius 150) with a wide dynamic range, and
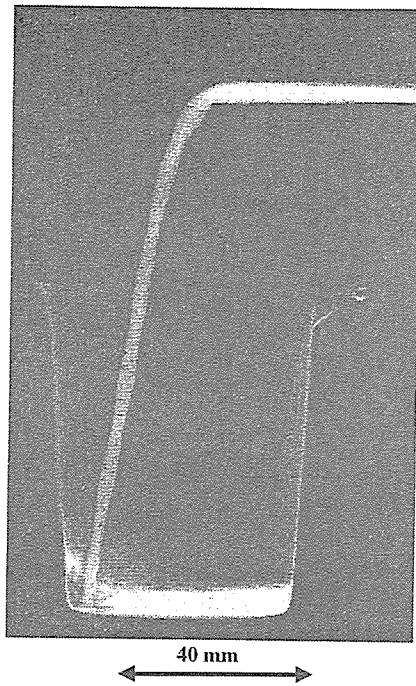
Fig. 9. Radiogram of water falling into polypropylene beaker from a glass test tube.
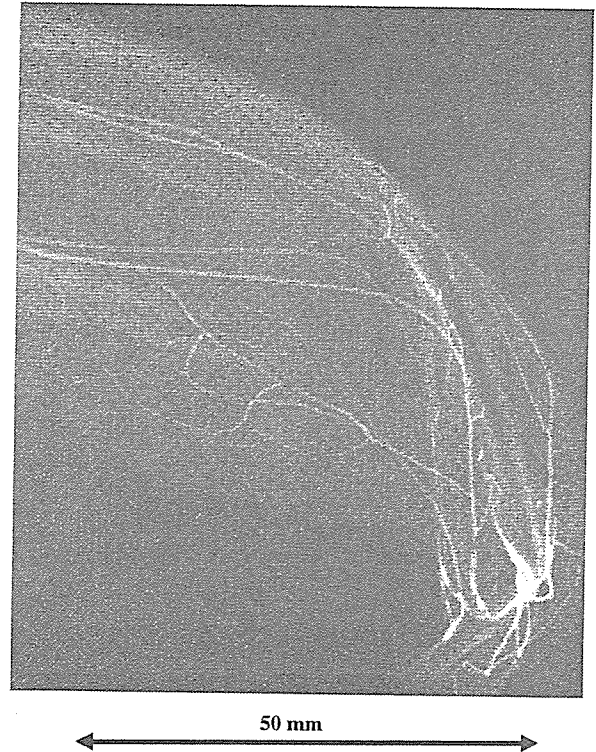

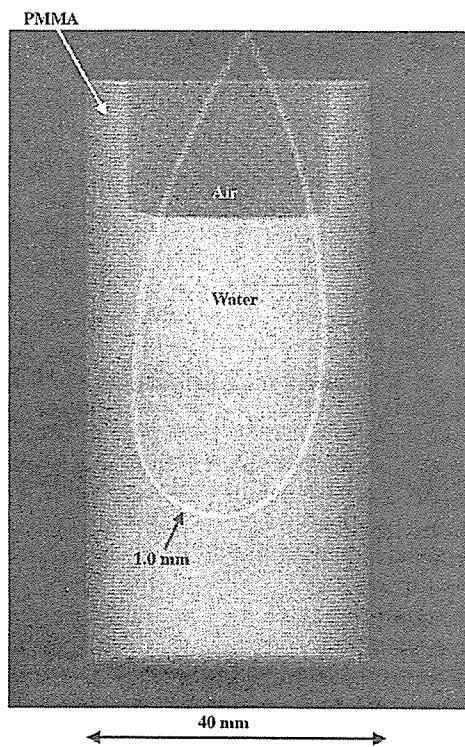Fig. 11. Angiography of a rabbit ear using gadolinium oxide powder.

relative X-ray intensity was calculated from Dicom original digital data corresponding to X-ray intensity; the data was scanned by Dicom viewer in the film-less CR system. Subsequently, the relative X-ray intensity as a function of the data was calibrated using a conventional X-ray generator, and we confirmed that the intensity was proportional to the exposure time. Fig. 7 shows measured spectra from the tungsten target. We observed clean K_α lines, while bremsstrahlung rays were hardly detected. The K_α intensity substantially increased with increases in the charging voltage.

5. Angiography

The flash angiography was performed by the CR system at 1.2 m from the X-ray source, and the charging voltage was 80 kV.

Firstly, rough measurements of spatial resolution were made using wires. Fig. 8 shows radiograms of tungsten wires coiled around rods made of polymethyl methacrylate (PMMA). Although the image contrast decreased somewhat with decreases in the wire diameter, due to blurring of the image caused by the sampling pitch of 87.5 μm, a 50-μm-diameter wire could be observed.

Fig. 10. Angiography of a Teflon tube using a contrast medium which contains approximately 65% gadodiamidehydrate.
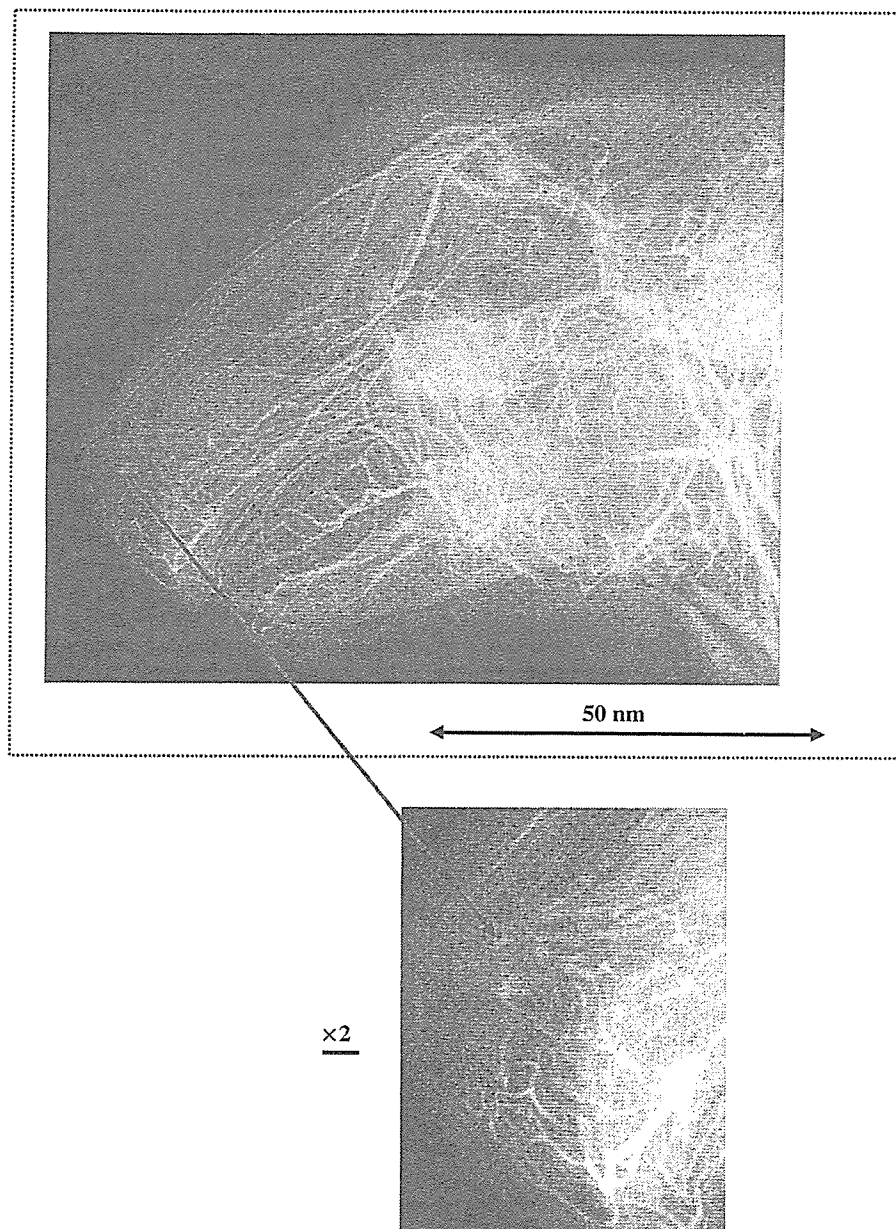
Fig. 12. Angiography of a rabbit head using gadolinium oxide powder.

The image of water (20% gadolinium oxide suspension) falling into a polypropylene beaker from a plastic test tube is shown in Fig. 9. The diameter of gadolinium oxide powder ranges from 1 to 10 μm. Because the X-ray duration was about 100 ns, the stop-motion image of water could be obtained.

Fig. 10 shows an angiogram of a polytetrafluoroethylene (Teflon) tube in a PMMA case using a contrast medium which contains approximately 65% gadodiamidehydrate, and a high-contrast tube with a bore diameter of 1.0 mm is observed. Figs. 11 and 12 show angiograms of a rabbit ear and head using gadolinium oxide powder, and fine blood vessels of approximately 100 μm were visible.

6. Conclusions and outlook

In summary, we succeeded in producing K_α rays of tungsten and in performing K-edge angiography using gadolinium contrast media with a K-edge of 50.2 keV, and this K-edge angiography could be a useful technique

to decrease the dose absorbed by patients. Although we employed tungsten K_α (58.9 keV) rays, L-series characteristic rays should be absorbed before angiography using a filter.

We obtained sufficient X-ray intensity for CR angiography with X-ray durations of approximately 100 ns, and the intensity can be increased by increasing the charging voltage at a constant target–cathode space. In an empirical equation, because the characteristic X-ray intensity is proportional to approximately 1.5th power of the voltage difference between the tube voltage and the critical excitation voltage, optimum intensity for angiography can be controlled. In this research, the generator produced instantaneous number of K photons was approximately 1×10^9 photons/cm^2 per pulse at 1.0 m from the source.

Because the dimensions of the X-ray source are primarily determined by the target diameter, the diameter should be minimized in order to improve the spatial resolution, and can be reduced to approximately 0.5 mm. Subsequently, the sampling pitch can be decreased to 43.8 μm using a CR system (Konica Minolta Regius 190) to observe fine blood vessels of approximately 50 μm diameter.

Using this flash X-ray generator, enhanced K-edge angiography using iodine contrast media can also be performed using a cerium target. In addition, steady-state monochromatic X-rays can be produced by a similar tube utilizing a hot cathode and a constant high-voltage power supply. In addition, fine focusing can be realized using tungsten or molybdenum target, and these X-ray generators could be employed to perform quasi-monochromatic phase-contrast radiography for edge enhancement.

Acknowledgments

References

Ando, M., Maksimenko, M., Sugiyama, H., Pattanasiriwisawa, W., Hyodo, K., Uyama, C., 2002. A simple X-ray dark- and bright-field imaging using achromatic Laue optics. Jpn. J. Appl. Phys. 41, L1016–L1018.

Davis, T.J., Gao, D., Gureyev, T.E., Stevenson, A.W., Wilkins, S.W., 1995. Phase-contrast imaging of weakly absorbing materials using hard X-rays. Nature 373, 595–597.

Hyodo, K., Ando, M., Oku, Y., Yamamoto, S., Takeda, T., Itai, Y., Ohtsuka, S., Sugishita, Y., Tada, J., 1998. Development of a two-dimensional imaging system for clinical applications of intravenous coronary angiography using intense synchrotron radiation produced by a multi-pole wiggler. J. Synchrotron Rad. 5, 1123–1126.

Momose, A., Takeda, T., Itai, Y., Hirano, K., 1996. Phase-contrast X-ray computed tomography for observing biological soft tissues. Nat. Med. 2, 473–475.

Mori, H., Hyodo, K., Tanaka, E., Mohammed, M.U., Yamakawa, A., Shinozaki, Y., Nakazawa, H., Tanaka, Y., Sekka, T., Iwata, Y., Honda, S., Umetani, K., Ueki, H., Yokoyama, T., Tanioka, K., Kubota, M., Hosaka, H., Ishizawa, N., Ando, M., 1996. Small-vessel radiography in situ with monochromatic synchrotron radiation. Radiology 201, 173–177.

Sato, E., Kimura, S., Kawasaki, S., Isobe, H., Takahashi, K., Tamakawa, Y., Yanagisawa, T., 1990. Repetitive flash X-ray generator utilizing a simple diode with a new type of energy-selective function. Rev. Sci. Instrum. 61, 2343–2348.

Sato, E., Takahashi, K., Sagae, M., Kimura, S., Oizumi, T., Hayasi, Y., Tamakawa, Y., Yanagisawa, T., 1994a. Sub-kilohertz flash X-ray generator utilizing a glass-enclosed cold-cathode triode. Med. Biol. Eng. Comput. 32, 289–294.

Sato, E., Sagae, M., Takahashi, K., Shikoda, A., Oizumi, T., Hayasi, Y., Tamakawa, Y., Yanagisawa, T., 1994b. 10kHz microsecond pulsed X-ray generator utilizing a hot-cathode triode with variable durations for biomedical radiography. Med. Biol. Eng. Comput. 32, 295–301.

Sato, E., Sato, K., Tamakawa, Y., 2000. Film-less computed radiography system for high-speed imaging. Ann. Rep. Iwate Med. Univ. Sch. Lib. Arts Sci. 35, 13–23.

Sato, E., Hayasi, Y., Germer, R., Tanaka, E., Mori, H., Kawai, T., Obara, H., Ichimaru, T., Takayama, K., Ido, H., 2003a. Irradiation of intense characteristic X-rays from weakly ionized linear molybdenum plasma. Jpn. J. Med. Phys. 23, 123–131.

Sato, E., Hayasi, Y., Germer, R., Tanaka, E., Mori, H., Kawai, T., Ichimaru, T., Takayama, K., Ido, H., 2003b. Quasi-monochromatic flash X-ray generator utilizing weakly ionized linear copper plasma. Rev. Sci. Instrum. 74, 5236–5240.

Sato, E., Sagae, M., Tanaka, E., Hayasi, Y., Germer, R., Mori, H., Kawai, T., Ichimaru, T., Sato, S., Takayama, Y., Ido, H., 2004a. Quasi-monochromatic flash X-ray generator utilizing a disk-cathode molybdenum tube. Jpn. J. Appl. Phys. 43, 7324–7328.

Sato, E., Hayasi, Y., Germer, R., Tanaka, E., Mori, H., Kawai, T., Ichimaru, T., Sato, S., Takayama, K., Ido, H., 2004b. Sharp characteristic X-ray irradiation from weakly ionized linear plasma. J. Electron Spectrosc. Related Phenom. 137–140, 713–720.

Sato, E., Tanaka, E., Mori, H., Kawai, T., Ichimaru, T., Sato, S., Takayama, K., Ido, H., 2004c. Demonstration of

enhanced K-edge angiography using a cerium target X-ray generator. Med. Phys. 31, 3017–3021.

Sato, E., Tanaka, E., Mori, H., Kawai, T., Ichimaru, T., Sato, S., Takayama, Y., Ido, H., 2005a. Compact monochromatic flash X-ray generator utilizing a disk-cathode molybdenum tube. Med. Phys. 32, 49–54.

Sato, E., Tanaka, E., Mori, H., Kawai, T., Sato, S., Takayama, Y., 2005b. High-speed enhanced K-edge angiography utilizing cerium plasma X-ray generator. Opt. Eng. 44, 049001–049016.

Sato, E., Tanaka, E., Mori, H., Kawai, T., Sato, S., Takayama, Y., 2005c. Clean monochromatic X-ray irradiation from weakly ionized linear copper plasma. Opt. Eng. 44, 049002–049016.

Shikoda, A., Sato, E., Sagae, M., Oizumi, T., Tamakawa, Y., Yanagisawa, T., 1994. Repetitive flash X-ray generator having a high-durability diode driven by a two-cable-type line pulser. Rev. Sci. Instrum. 65, 850–856.

Takahashi, K., Sato, E., Sagae, M., Oizumi, T., Tamakawa, Y., Yanagisawa, T., 1994. Fundamental study on a long-duration flash X-ray generator with a surface-discharge triode. Jpn. J. Appl. Phys. 33, 4146–4151.

Thompson, A.C., Zeman, H.D., Brown, G.S., Morrison, J., Reiser, P., Padmanabahn, V., Ong, L., Green, S., Giacomini, J., Gordon, H., Rubenstein, E., 1992. First operation of the medical research facility at the NSLS for coronary angiography. Rev. Sci. Instrum. 63, 625–628.

Enhanced real-time magnification angiography utilizing a 100-μm-focus x-ray generator in conjunction with an image intensifier

Eiichi Sato*[a], Etsuro Tanaka[b], Hidezo Mori[c], Toshiaki Kawai[d], Takashi Inoue[e], Akira Ogawa[e], Mitsuru Izumisawa[f], Kiyomi Takahashi[g], Shigehiro Sato[g], Toshio Ichimaru[h] and Kazuyoshi Takayama[i]

[a]Department of Physics, Iwate Medical University, 3-16-1 Honchodori, Morioka 020-0015, Japan
[b]Department of Nutritional Science, Faculty of Applied Bio-science, Tokyo University of Agriculture, 1-1-1 Sakuragaoka, Setagaya-ku 156-8502, Japan
[c]Department of Cardiac Physiology, National Cardiovascular Center Research Institute, 5-7-1 Fujishirodai, Suita, Osaka 565-8565 Japan
[d]Electron Tube Division #2, Hamamatsu Photonics K.K., 314-5 Shimokanzo, Iwata 438-0193, Japan
[e]Department of Neurosurgery, School of Medicine, Iwate Medical University, 19-1 Uchimaru, Morioka 020-8505, Japan
[f]Department of Oral Radiology, School of Dentistry, Iwate Medical University, 1-3-27 Chuo, Morioka 020-0021, Japan,
[g]Department of Microbiology, School of Medicine, Iwate Medical University, 19-1 Uchimaru, Morioka 020-8505, Japan
[h]Department of Radiological Technology, School of Health Sciences, Hirosaki University, 66-1 Honcho, Hirosaki 036-8564, Japan
[i]Tohoku University Biomedical Engineering Research Organization, Tohoku University, 2-1-1 Katahira, Sendai 980-8577, Japan

ABSTRACT

A microfocus x-ray tube is useful in order to perform magnification digital radiography including phase-contrast effect. The 100-μm-focus x-ray generator consists of a main controller for regulating the tube voltage and current and a tube unit, with a high-voltage circuit and a fixed anode x-ray tube. The maximum tube voltage, current, and electric power were 105 kV, 0.5 mA, and 50 W, respectively. Using a 3.0-mm-thick aluminum filter, the x-ray intensity was 26.0 μGy/s at 1.0 m from the source with a tube voltage of 60 kV and a current of 0.50 mA. Because the peak photon energy was approximately 35 keV using the filter with a tube voltage of 60 kV, the bremsstrahlung x-rays were absorbed effectively by iodine-based contrast media with an iodine K-edge of 33.2 keV. Real-time magnification radiography was performed by twofold magnification imaging with an image intensifier camera, and angiography was achieved with iodine-based microspheres 15 μm in diameter. In angiography of non-living animals, we observed fine blood vessels of approximately 100 μm with high contrasts.

Keywords: real-time magnification radiography, magnification angiography, 100-μm-focus tube, tungsten target, image intensifier, phase-contrast effect

1. INTRODUCTION

To perform high-speed biomedical radiography, several various flash x-ray generators using cold-cathode tubes have

been developed.[1-4] In particular, quasi-monochromatic flash x-ray generators[5-10] have been designed to perform preliminary experiments for producing clean K-series x-rays, and higher-harmonic hard x-rays have been observed in a weakly ionized linear plasma of copper and nickel. However, in monochromatic flash radiography, difficulties in increasing x-ray duration and in performing x-ray computed tomography (CT) have been encountered. In view of this situation, we have developed steady-state characteristic x-ray generators to produce clean characteristic x-rays, since bremsstrahlung rays are not emitted in the opposite direction to that of electron trajectory.

Monochromatic parallel beams produced from a synchrotron using silicon crystals have been employed in phase-contrast radiography[11,12] and enhanced K-edge angiography.[13,14] In particular, the parallel beams with photon energies of approximately 35 keV have been employed to perform iodine K-edge angiography, because the beams are absorbed effectively by iodine-based contrast media with a K-absorption edge of 33.2 keV.

Without using synchrotrons, phase-contrast radiography for edge enhancement can be performed using a microfocus x-ray tube, and the magnification radiography including the phase-contrast effect[15] has been applied in mammography achieved with a computed radiography (CR) system[16] (Regius 190, Konica Minolta) with a sampling pitch of 43.8 μm using a 100-μm-focus molybdenum tube. Subsequently, we have developed a cerium x-ray generator[17-19] to perform enhanced K-edge angiography using cone beams, and have succeeded in observing fine blood vessels and coronary arteries with high contrasts using cerium Kα rays of 34.6 keV. However, it is difficult to design a small focus cerium tube for angiography.

Magnification radiography is useful in order to improve the spatial resolution in digital radiography, and narrow photon energy bremsstrahlung x-rays with a peak energy of approximately 35 keV from a microfocus tungsten tube are useful to perform high-contrast high-resolution angiography. In magnification radiography, scattering beams from radiographic objects can be reduced without using a grid.

In this research, we employed a 100-μm-focus tungsten tube, used to perform real-time magnification radiography, including angiography, using an image intensifier (II) in conjunction with a CCD camera.

2. X-RAY GENERATOR

Figure 1 shows the block diagram of a microfocus x-ray generator used in this experiment, and the generator consists of a main controller, an x-ray tube unit with a Cockcroft-Walton circuit, an insulation transformer, and a 100-μm-focus x-ray tube. The tube voltage, the current, and the exposure time can be controlled by the controller. The main circuit for producing x-rays employs the Cockcroft-Walton circuit in order to decrease the dimensions of the tube unit. In the x-ray tube, the positive and negative high voltages are applied to the anode and cathode electrodes, respectively. The filament heating current is supplied by an AC power supply in the controller in conjunction with an insulation transformer which is used for isolation from the high voltage from the Cockcroft-Walton circuit. In this experiment, the tube voltage applied was from 45 to 70 kV, and the tube current was regulated to within 0.50 mA (maximum current) by the filament temperature. The exposure time is controlled in order to obtain optimum x-ray intensity, and narrow-photon-energy bremsstrahlung x-rays are produced using a 3.0-mm-thick aluminum filter for absorbing soft x-rays.
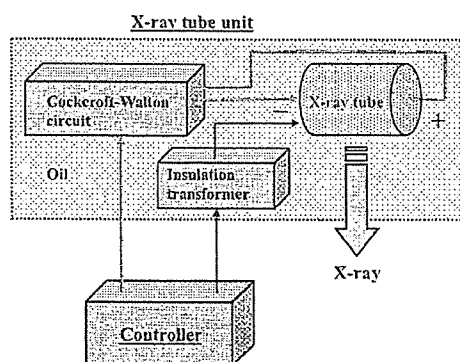

Fig. 1. Block diagram of the x-ray generator.

3. RESULTS AND DISCUSSION

3.1 X-ray intensity

The x-ray intensity was measured by a Victoreen 660 ionization chamber at 1.0 m from the x-ray source using the filter (Fig. 2). At a constant tube current of 0.50 mA, the x-ray intensity increased when the tube voltage was increased. At a tube voltage of 60 kV, the intensity with the filter was 26.0 μGy/s.

3.2 X-ray Spectra

In order to measure x-ray spectra, we employed a cadmium telluride detector (XR-100T, Amptek) (Fig. 3). When the tube voltage was increased, the bremsstrahlung x-ray intensity increased, and both the maximum photon energy and the spectrum peak energy increased.

In order to perform K-edge angiography, bremsstrahlung x-rays of approximately 35 keV are useful, and the high-energy bremsstrahlung x-rays decrease the image contrast. Using this filter, because bremsstrahlung x-rays with energies higher than 60 keV were not absorbed easily, the tube voltage for angiography was determined as 60 kV by considering the filtering effect of radiographic objects.
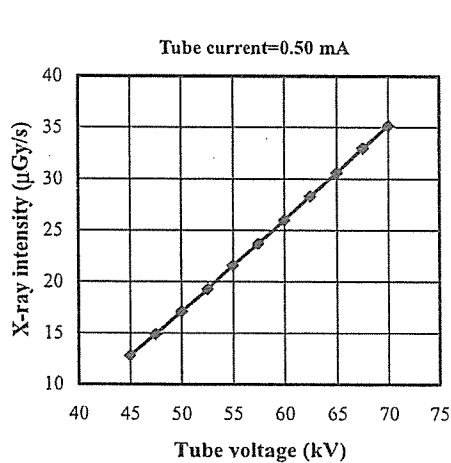
Fig. 2. X-ray intensity (μGy/s) as a function of tube voltage (kV) with a tube current of 0.50 mA.
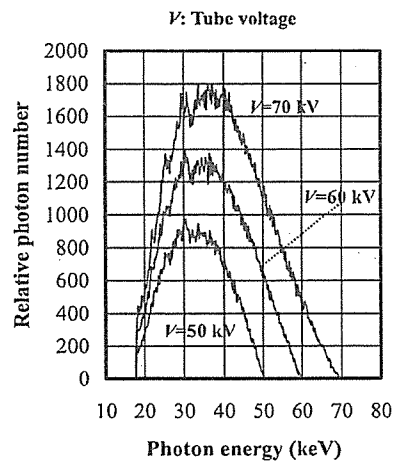
Fig. 3. Bremsstrahlung x-ray spectra measured using a cadmium telluride detector with changes in the tube voltage.

3.3 Magnification radiography

The magnification radiography was performed by twofold magnification imaging using the II camera and the filter at a tube voltage of 60 kV, and the distance between the x-ray source and the II was 1.0 m (Figs. 4 and 5). First, the spatial resolution of magnification radiography was made using a lead test chart (Fig. 6). In the magnification radiography, 109 μm lines (4.6 line pairs/mm) were visible. Subsequently, radiography of tungsten wires coiled around rods made of polymethyl methacrylate (PMMA) was performed (Fig. 7). Although the image contrast decreased somewhat with decreases in the wire diameter, a 50-μm-diameter wire could be observed.
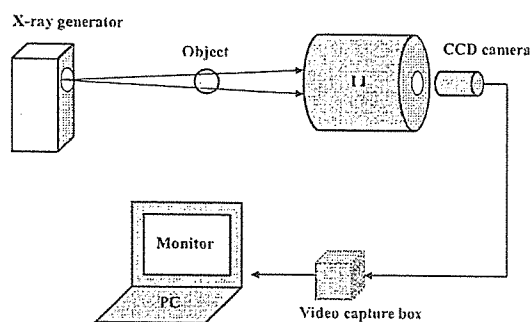
Fig. 4. Real-time magnification imaging using an image intensifier camera (low-resolution mode) in conjunction with a microfocus tube.
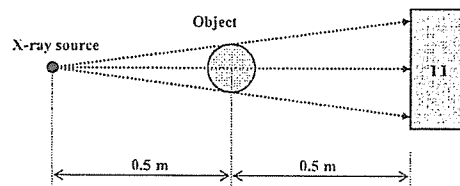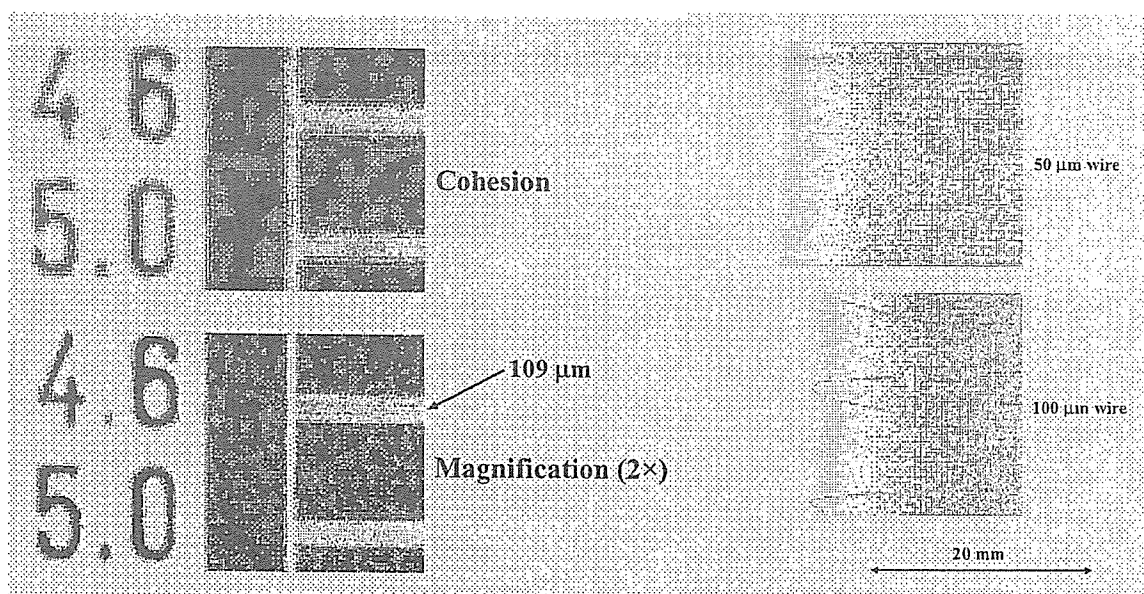

Fig. 5. Twofold magnification imaging.

Cohesion

109 μm

Magnification (2×)

50 μm wire

100 μm wire

20 mm

Fig. 6. Radiograms of a test chart for measuring the spatial resolution.

Fig. 7. Radiograms of tungsten wires coiled around PMMA rods.

3.4 Enhanced magnification angiography

Figure 8 shows the mass attenuation coefficients of iodine at the selected energies; the coefficient curve is discontinuous at the iodine K-edge. The effective bremsstrahlung x-ray spectra for K-edge angiography are shown above the iodine K-edge. Because iodine contrast media with a K-absorption edge of 33.2 keV absorb the rays easily, blood vessels were observed with high contrasts.

The magnification angiography was performed at the same conditions using iodine microspheres of 15 μm in diameter, and the microspheres (containing 37% iodine by weight) are very useful for making phantoms of non-living animals used for angiography. Angiograms of a rabbit heart on the turn table is shown in Fig. 9, and the coronary arteries are visible. Figure 10 shows angiograms of a dog heart in an xy table, and blood vessels of approximately 100 μm in diameter were observed.

4. CONCLUSION AND OUTLOOK

We employed an x-ray generator with a 100-μm-focus tungsten tube and performed real-time magnification radiography (fluoroscopy) using the II camera. To perform angiography, we employed narrow-photon-energy bremsstrahlung x-rays with a peak photon energy of approximately 35 keV, which can be absorbed easily by iodine-based contrast media. The bremsstrahlung x-ray intensity substantially increased with increases in the tube voltage, and the tube voltage was determined as 60 kV in order to increase the image contrast by decreasing high-photon-energy bremsstrahlung x-rays with energies beyond 60 keV. In enhanced angiography, low-photon-energy bremsstrahlung rays should be absorbed by an aluminum filter. Although we obtained mostly absorption-contrast images, the phase-contrast effect may be added in cases where low-density media are employed.

We obtained spatial resolutions of approximately 110 μm using twofold magnification imaging using the II even when a 100-μm-focus tube was employed. In order to observe fine blood vessels of less than 100 μm, the spatial resolution of the radiography system should be improved to approximately 50 μm using the II driven in a high-resolution mode, and the iodine density should be increased. At a tube voltage of 60 kV and a current of 0.50 mA, the photon number was approximately 4×10^7 photons/$(cm^2 \cdot s)$ at 1.0 m from the source, and photon count rate can be increased easily using a rotating anode microfocus tube developed by Hitachi Medical Corporation. Because the focus diameter of the tube has been decreased to 10 μm, a high-resolution real-time magnification radiography system will become possible.
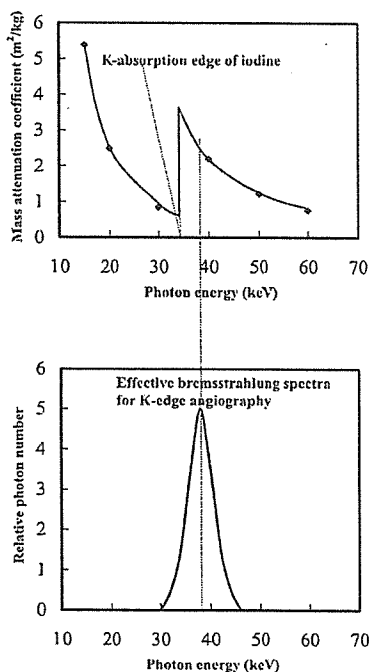

Fig. 8. Mass attenuation coefficients of iodine and effective bremsstrahlung x-rays for enhanced K-edge angiography.
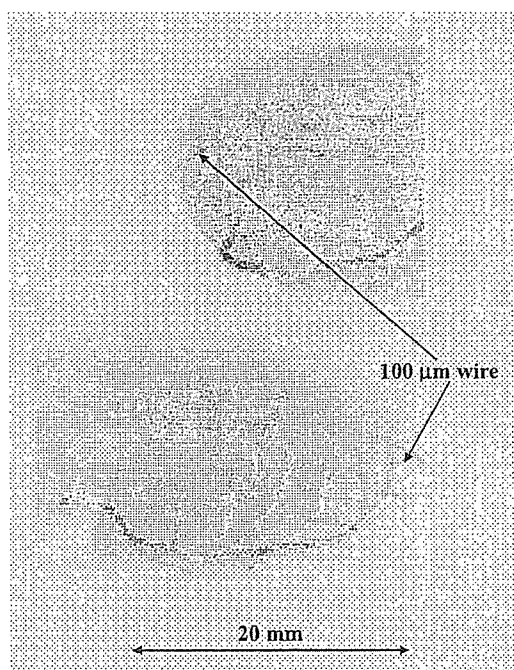

Fig. 9. Angiogram of an extracted rabbit heart using iodine microspheres.